Dynamic impedance spectroscopy of $LiMn_2O_4$ thin films made by multi-layer pulsed laser deposition.

C. Erinmwingbovo[a], V. Siller[b], M. Nuñez[b], R. Trócoli[c], D. Brogioli[a], A. Morata[b,*], F. La Mantia[a,**]

[a] *Universitt Bremen, Energiespeicher- und Energiewandlersysteme, Bibliothekstr. 1, 28359 Bremen, Germany.*
[b] *IREC, Jardins de les Dones de Negre 1, 2a, 08930 Sant Adriá de Besós, Barcelona, Spain.*
[c] *Institut de Ciéncia de Materials de Barcelona (ICMAB-CSIC), Campus UAB, Bellaterra, Catalonia, E-08193, Spain.*

Abstract

The kinetics of the reversible insertion of lithium ions assisted by aqueous environment into $LiMn_2O_4$ thin film fabricated by multi-layer pulsed laser deposition is studied using dynamic multi-frequency analysis (DMFA). This method allowed us to acquire time resolved impedance spectra in the range of 210 kHz to 11.5 Hz during cyclic voltammetry. The impedance spectra obtained comprises of two RC time constants (semi-circles) indicating that the reversible insertion process of lithium ions in $LiMn_2O_4$ thin films in aqueous media follows a two-stage intercalation process with the first stage as the (de)solvation step of the lithium ions and the second stage as a (de)insertion process with a concurrent change in the oxidation state of manganese. The temporal development of the kinetic parameters with the state of charge during the voltage sweep was investigated and reported in this work.

Keywords: $LiMn_2O_4$ thin films, interfacial lithium ion transfer, multi-layer pulse laser deposition, multi-frequency analysis, dynamic impedance spectroscopy.

1. Introduction

Recently, the interest in thin film batteries for micro devices has pushed researchers to investigate and develop thin film cathode and anode materials with desirable features such as cost effectiveness, environment-friendly, high energy density, high power density and high rate capability [1, 2, 3, 4, 5, 6]. $LiMn_2O_4$ has been reported by several research groups as a promising cathode material for thin film batteries as it possesses most of the above listed properties. In addition to that, $LiMn_2O_4$ thin films have other advantages such as the ability of improving the electrochemical performances by controlling the phase and micro-structure of the thin films through the adaptation of deposition parameters, such as temperature, background pressure, target-to-substrate distance and the substrate itself [5, 7, 8, 9, 10, 11, 12, 13, 14, 15]. $LiMn_2O_4$ thin films have also been reported to overcome the challenges associated with powder $LiMn_2O_4$ such as

*Corresponding author.
Email address: amorata@irec.cat
**Corresponding author.
Email address: lamantia@uni-bremen.de

instability due to manganese dissolution [1, 16, 17] making them an attractive candidate as a cathode material.

Feshe et.al. reported $LiMn_2O_4$ thin films deposited on Si-based substrate with Pt current collector via multi-layer pulse laser deposition (PLD) approach [1]. The layers exhibited high reversibility and outstanding electrochemical performance in aqueous media. At high C-rate (348 C), the thin films demonstrated a long time (3500 cycles) operation maintaining coulombic efficiency of 99.996% [1] higher than what has been reported by other research groups such as Singh et al. 99.986% per cycle for 1100 cycles at 18 C [11] and Tang et al. 99.981% per cycle for 500 cycles at 18 C [6]. A battery comprising of $LiMn_2O_4$ thin films made by the multi-layer PLD approach as cathode material and zinc as anode in mixed aqueous electrolyte medium comprising of Zn and Li ions was recently reported by Trócoli et.al [18]. The battery exhibited a specific power density of 3400 W kg^{-1} while maintaining specific energies in the range of typical Li-ion batteries (Ca. 100 Wh kg^{-1}) and a coulombic efficiency of 99.94% over 300 cycles [18]. For high energy and power applications, a facile intercalation process is desired for cathode materials. Thus, understanding the mechanism of de-insertion process and the temporal development of kinetic parameters as a function of the state of charge of the cathode materials plays an important part in optimization and development of cathode materials for battery applications. The kinetics of reversible insertion of Li^+ in $LiMn_2O_4$ in non-aqueous solvents have been extensively studied and reported in literature [11, 19, 20, 21]. On the other hand, a satisfactory investigation of the kinetics of the reversible insertion of Li^+ in $LiMn_2O_4$ in aqueous medium is still missing to the best of our knowledge. In cases where an attempt has been made, the kinetics were studied in stationary conditions neglecting the evolution of the kinetic parameters on the state of charge of the $LiMn_2O_4$ [20, 22].

For studying the kinetics during non-stationary process, our research group recently reported the acquisition of dynamic electrochemical impedance spectroscopy under non-stationary conditions using dynamic multi frequency analysis (DMFA) [23, 24, 25]. In addition to the advantage of fast computational time offered by DMFA compared to other methods of acquiring dynamic impedance spectroscopy [26, 27, 28, 29, 30, 31, 32], it also differs from the widely used fast Fourier transformation electrochemical impedance spectroscopy (FFT-EIS) that is based on windows method by the use of digital filters which are more general in shape in the time domain [25, 24]. Unlike FFT-EIS which suffers from poor bandwidth of the window function, in DMFA the maximum value of the bandwidth can be calculated from the design of the multi-sine allowing for separation of the individual voltage perturbation and the current response for each fundamental frequency [25]. More details of the physical definition, similarities and difference of both methods can be found in [25].

In this paper, we study the kinetics of the reversible insertion of Li^+ in $LiMn_2O_4$ thin films made by multi-layer PLD approach using dynamic multi-frequency analysis. DMFA allows for the acquisition of time resolved impedance during a non-stationary process [23, 25, 24, 33, 34], in this case caused by a voltage sweep corresponding to a quasi cyclic voltammetry [24]. This allows for the investigation of the temporal development of the kinetic parameters on the state of charge while cycling leading to a better understanding of the mechanism of intercalation [23, 25, 24, 33, 34]. DMFA also has an added advantage in reduction of the time required to acquire impedance as the system is perturbed at a specified time interval during the voltage sweep with predefined frequencies. This is advantageous for electrochemical systems which are unstable and may undergo irreversible changes and/or degradation during the longer time needed to acquire a large amount of impedance data in large potential window.

2. Experimental

2.1. Deposition of $LiMn_2O_4$ thin film

$LiMn_2O_4$ thin films were prepared using PLD5000 by PVD Products Inc. equipped with KrF excimer laser with 248 nm wavelength and $LiMn_2O_4$ and Li_2O targets purchased from Neyco, France. Films were deposited onto Pt and TiN coated silicon substrates provided by IMEC. The deposition temperature, target-substrate distance, and frequency were fixed at 650°C, 90 mm, and 10 Hz respectively. Alternating ablation of the $LiMn_2O_4$ and Li_2O target was repeated over 30 cycles at an oxygen background pressure of 20 mTorr leading to a final film thickness of 200 nm. A detailed description of the deposition method and conditions can be found in previous publications [18, 35]. X-ray diffraction (XRD) measurement on the $LiMn_2O_4$ thin films were conducted using Bruker-D8 advance equipment using CuKα radiation with a Ni filter and Lynx Eye. XRD spectra were collected in a 2θ range between 10° and 65° in order to avoid the main peak of the (100) oriented single crystal silicon substrate. The SEM equipment used is a Zeiss Auriga equipped with Inlens and back scattered electron detector.

2.2. Electrochemical measurements

Electrochemical experiments were done in a there-electrode cell set-up using the co-axial configuration [1, 36, 37] with the $LiMn_2O_4$ film as the working electrode(WE) and a platinum mesh (Labor Platina) as the counter electrode (CE). The reference electrode (RE) was a capacitively-coupled low-impedance Ag/AgCl (3M KCl) reference electrode which is able to avoid or decrease high frequency artefacts coming from the series resistance of the RE [36]. In our case, the series resistance of standard Ag/AgCl reference electrode alone was of the order of 1 kΩ. We fabricated our low-impedance reference electrode by coiling a 0.1 mm platinum wire around the tip of the reference electrode and connecting it through a 100 nF capacitor to the Ag/AgCl wire [38]. This allows us to decrease the impedance to around 20 Ω, to remove possible artefacts. The electrolyte used in this work was 1 M Li_2SO_4 and all electrochemical experiments were carried out at room temperature.

DMFA was implemented in this work by the superimposition of quasi-triangular wave which represents the voltage sweep and a multi-sine wave. The frequency of the quasi-triangular wave was chosen to be 10 mHz with an amplitude of 400 mV peak to peak corresponding to a scan rate of 16 mVs^{-1}. The base frequency for the multi-sine was 0.5 Hz and its amplitude (ΔU_{ac}) was 100 mV peak to peak, selected as a compromise between linearity and high signal-to-noise ratio. The current output from the potential perturbation indicates that the system is linear with the amplitude used (100 mVpp) as the second harmonics had negligible intensity in the Fourier domain (see Fig. S1 in the supporting information for one of the frequencies, namely 1.5 Hz). The potential perturbation comprised of 45 optimized frequencies in six decades selected using the criteria reported by Koster et.al. [24] resulting in the dynamic impedance been captured within the frequency range of 500 kHz to 0.5 Hz. The current range was set at 100 mA for the VS-300 Bio-Logic potentiostat. The voltage perturbation and current output were measured using a two-channel oscilloscope 4262 PicoScope (Pico technology). The data were analyzed using a home-made MATLAB script. From the resulting time-series of spectra evaluated by DMFA, we selected 100 spectra in the cathodic scan and 100 spectra in the anodic scan. More details of the implementation of DMFA and the data extraction can be found in publications of our research group [23, 24, 33].

3. Results and discussion

3.1. Structural characterization

The thin films were prepared by PLD multi-layer approach consisting of alternating $LiMn_2O_4$ and Li_2O layer deposition with the aim to compensate for the loss of lithium during deposition [39]. Fig. 1 shows the X-ray diffractogram obtained from the film in comparison to the signal detected from the plain substrate. The main evidence showing the presence of the $LiMn_2O_4$ phase is provided by the peak corresponding to the (111) plane of spinel $LiMn_2O_4$ (JCPDS 00-035-782) at $2\theta = 18.61°$. This could be an indication for a preferential crystal orientation, which was already reported in previous works [18]. The presence of a shoulder towards lower diffraction angles on the (111) peak was attributed to small amounts of Mn_3O_4(JCPDS 01-080-0382) in similar layers [1, 18]. Additionally, it can also be the result from a slight shift in the peak position due to the presence of multiple $LiMn_2O_4$ phases with small deviations from the stoichiometric Li:Mn ratio, as it was observed in the past for different PLD fabricated layers [11, 40].

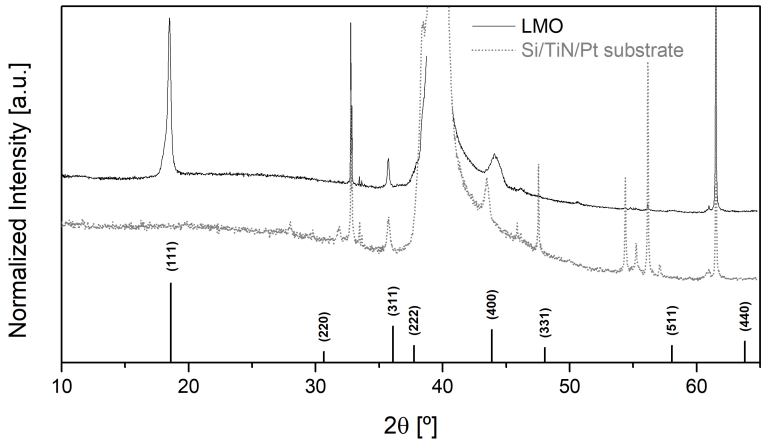

Figure 1: XRD diffractogram of the 200 nm thick multi-layer deposited thin film and the ascribed spinel phase $LiMn_2O_4$ (JCPDS 00-035-782) indicated in the plot with its corresponding (hkl).

SEM pictures shown in Fig. 2 indicate mostly elongated grains with random orientation towards each other, forming a dense layer on top of the platinum as demonstrated in the cross-section. Therefore, the multi-layer approach in the PLD is proven to be reproducible in respect of previous works [1, 35]. The thickness of the deposited film was estimated to be 200 nm using cross-sectional FIB-SEM.

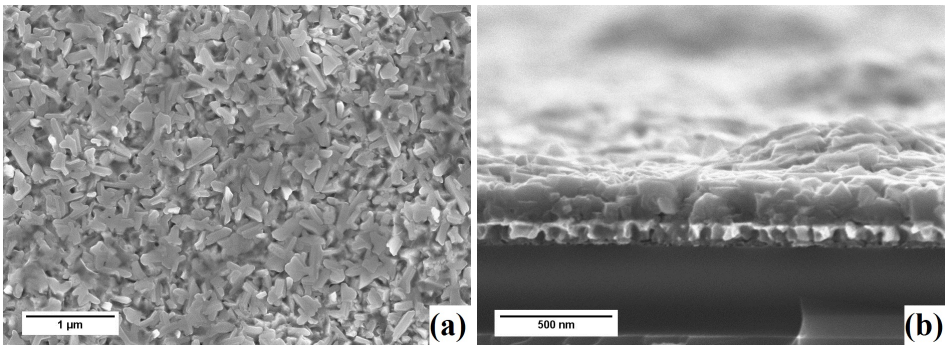

Figure 2: SEM images of the (a) top view and (b) cross-sectional view of the deposited 200 nm $LiMn_2O_4$ thin film.

3.2. Quasi cyclic voltammetry

The voltammogram obtained from the application of the voltage sweep to the 200 nm $LiMn_2O_4$ films is shown in Fig. 3. The same voltage sweep was applied in all the experiments for the application of DMFA. The two peaks associated with the reversible insertion of Li^+ in $LiMn_2O_4$ was observed in the voltammogram. It has been reported that the reversible insertion of Li^+ in $LiMn_2O_4$ occurs in several steps [41, 42, 43].

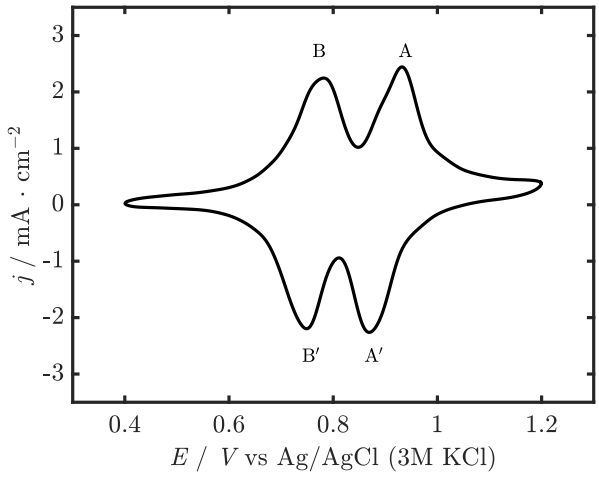

Figure 3: Voltammogram obtained from the quasi-triangular wave applied to 200 nm $LiMn_2O_4$ thin film in 1 M Li_2SO_4 solution at a scan rate of 16 mVs^{-1}.

In the redox process $A - A'$, Li^+ is inserted into two phases which coexist as lithium-poor and lithium-rich phase between lithium concentration ratio of 0 to 0.10 and 0.10 to 0.35 respectively [42]. As the lithiation process continues, the chemical potential of Li^+ (μ_{Li}) in the $LiMn_2O_4$ decrease until half the 8a sites are filled up which occurs around lithium concentration ratio of 0.5. Further insertion Li^+ continues in this new solid solution with a different μ_{Li} until all 8a sites are filled [42]. The peak separation ΔE_p for the peak pairs A/A' and B/B' was observed

to be 40 mV and 60 mV respectively at a scan rate of 16 mVs^{-1} indicating fast charge transfer kinetics [34, 44, 45, 46].

3.3. Dynamic impedance spectroscopy

One of the heuristic definitions of dynamic impedance Z' is given by [25, 24]:

$$Z' = \frac{iFT[\Delta U(\omega).g(\omega' - \omega), bw]}{iFT[\Delta I(\omega).g(\omega' - \omega), bw]} \tag{1}$$

where ΔU and ΔI are the Fourier transform of the potential and current signals respectively, ω is the angular frequency, g is a quadrature filter function, and bw is the bandwidth of the quadrature filter. Detailed explanation about the choice of the filter function and bandwidth can be found in previous publications from our research group [23, 25, 24].

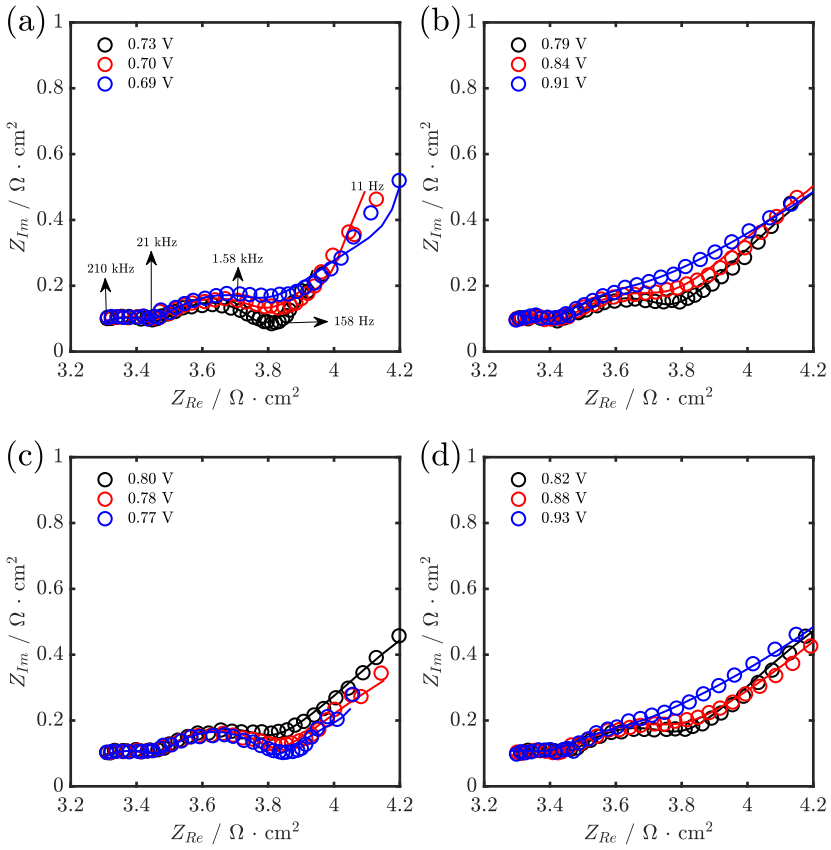

Figure 4: Nyquist plot of impedance spectra of $LiMn_2O_4$ films in 1 M Li_2SO_4 within the frequency range of 210 kHz to 11.5 Hz at different potentials during (a) and (b) cathodic scan (c) and (d) anodic scan. The ○ represents the experimental data while — represents the data from the model.

The extracted impedance spectra shown in this work contained 35 frequencies within a frequency range 11.5 Hz to 210 kHz of the 45 frequencies acquired. The very high frequency data

points (500 kHz to 281 kHz) were discarded due to the high frequency artefacts which could arise from the stray capacitance of the cable connected to the potentiostat and to the input capacitance of potentiostat occurring at very high frequencies while the very low frequency data (9.5 Hz to 0.5 Hz) points were discarded due to the quality of low frequency data points which were noisy.

The impedance spectra obtained comprises of two semi-circle in the high and medium frequency range terminated by a straight line occurring at the low frequency region as seen in Fig. 4. This straight line occurring at an angle of less than 90° has been associated with the mass transport of cations in porous host structure [47]. The complex plane plots suggests a deviation from the pristine finite length diffusion shape due to the absence of a well defined transition zone between the Warburg behaviour and capacitive behaviour of the spectra. This deviation can be attributed to particle size distribution. Heterogeneous particle size distribution results in frequency dispersion and the transition which is characteristic of finite diffusion spreads over a wide range of frequency [48].

The experimental impedance spectra suggests that the reversible insertion of Li^+ in $LiMn_2O_4$ thin films made by multi-layer PLD in 1 M Li_2SO_4 is a two-stage intercalation process similar to what has been reported for other cathode materials in aqueous and non-aqueous electrolyte [49, 50, 51, 52, 53]. The first stage involves the sorption of lithium in solution (Li^+_ε) which corresponds to the removal of parts of the solvation shell and the formation of adsorbed lithium ions in the inner Helmholtz plane (IHP) (Li^+_i) as shown below:

$$Li^+_\varepsilon \rightleftharpoons Li^+_i \tag{2}$$

The second step of the (de)insertion process corresponds to the reversible insertion of the adsorbed lithium ions (Li^+_i) into λ–$LiMn_2O_4$ and the subsequent change in the oxidation state of Mn. During the insertion, the composition changes from Mn_2O_4 to $Li_2Mn_4O_8$; at the composition $Li_2Mn_4O_8$, a phase transition takes place. A simplified but effective modelling of the process is done by considering the insertion into Mn_2O_4 and $LiMn_4O_8$ as two separate reactions:

$$Li_i{}^+ + \lambda\text{–}Mn_4O_8 + e^- \rightleftharpoons LiMn_4O_8 \tag{3}$$

$$Li_i{}^+ + LiMn_4O_8 + e^- \rightleftharpoons Li_2Mn_4O_8 \tag{4}$$

Considering the primitive cell of the LMO consisting of 14 atoms [54], $Li_2Mn_4O_8$, the reaction 3 takes place until one of the two free sites of each cell are occupied by a Li^+ ion; then the insertion of further Li^+ takes place according to reaction 4.

3.4. Equivalent circuit

The impedance (Z) of the two-stage intercalation is given by [34]:

$$\frac{1}{Z} \approx \frac{\gamma^2(R_{ad}+Z_{Wad})+(1-\gamma)^2(R_{ct}+Z_{Wct})+\left(\frac{1}{j\omega C_{ad}}+\frac{\gamma(1-\gamma)}{j\omega C_{dl}}\right)}{(R_{ct}+Z_{Wct})(R_{ad}+Z_{Wad})+(R_{ct}+Z_{Wct}+R_{ad}+Z_{Wad})\left(\frac{1}{j\omega C_{ad}}+\frac{\gamma(1-\gamma)}{j\omega C_{dl}}\right)}+j\omega C_{dl} \tag{5}$$

where R_{ad}, Z_{Wad} and C_{ad} represents resistance due to adsorption (correlated to eq. 2), mass transport in the electrolyte described using semi-infinite diffusion and adsorption capacitance respectively. R_{ct} is the charge transfer resistance (correlated to eq. 3 or eq. 4 depending on the state of charge), Z_{Wct} denotes the mass transport of the cations in the solid described using finite

length diffusion and C_{dl} denotes the capacitance of the double layer which is described as the series combination of the capacitance of the outer Helmholtz plane (C_1) and capacitance in the inner Helmholtz plane (C_2). $\gamma = C_1/(C_1 + C_2)$ and $1 - \gamma = C_2/(C_1 + C_2)$. A brief description of the model can be found in the supporting information and detailed mathematical description of the two-stage intercalation model can be found in the supporting information of our previous publication [34]. The circuit shown in Fig. 5a is equivalent to Eq. 5: this can be easily proven by calculating the impedance of the circuit by the nodal method.

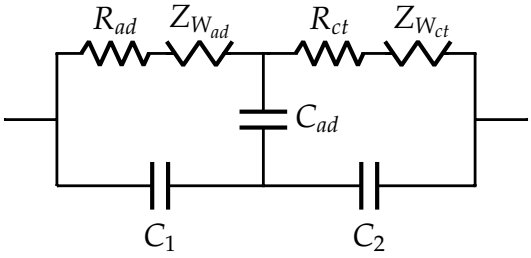

Figure 5: Equivalent circuit obtained from modelling the reversible insertion of lithium in aqueous medium as two-stage process

Since the impedance was acquired in a three-electrode cell configuration, the total impedance ($Z_T(\omega)$) is described as $Z_T(\omega) = R_u + Z_{WE}(\omega)$, where R_u is the uncompensated cell resistance which is part of the solution resistance left uncompensated by the placement of RE in a three-electrode cell and $Z_{WE}(\omega)$ is the impedance of the working electrode (LMO film). The impedance of the LMO film were fitted using the simplified transmission line model (TLM) for describing cylindrical pores with the equivalent circuit is shown in Fig. 6 [55]:

$$Z_{WE}(\omega) = R_p \left[\frac{\coth(\kappa d)}{\kappa d} \right] \tag{6}$$

R_p is the resistance of the pores, κd corresponds to the impedance of single reacting sites (Z) and is described as [55]:

$$\kappa d = \sqrt{\frac{R_p}{Z}} \tag{7}$$

The decision to use the TLM was based on the shape of the impedance spectra at high frequency region and the SEM images (Fig. 2) which show that the films are porous and made of randomly oriented grains. The modified non-linear least squares minimization objective function reported in [23] was used for the selected 200 impedance spectra to the model. The fitting of the measured impedance with the equivalent circuit obtained from the model inserted to the TLM (Fig. 6) resulted in a good fit with a χ^2 of $5.23 \cdot 10^{-5}$. However, the t-test showed that the value of some of the parameters were below the confidence interval used in this work (95% confidence level) as shown in Fig. S2a in the supporting information.

A good fit with a χ^2 value of $3.2 \cdot 10^{-5}$ shown in Fig. 4 where the continuous line is the impedance from the model and all parameters above the confidence level was obtained using the equivalent circuit shown in Fig. 7. It is important to highlight that no constant phases elements were used in the fitting procedure. In order to pass from the equivalent circuit in Fig. 6 to the

equivalent circuit in Fig. 7, the following assumptions on the model were done: (i) the adsorption capacitance is higher than capacitance of the IHP thus C_{ad} can be treated as a short circuit. Using probable values of C_{ad}, the effect of C_{ad} on impedance is illustrated in the supporting information. (ii) the mass transport in the liquid phase is fast enough to be negligible. Detailed description of the statistical analysis is reported in the supporting information.

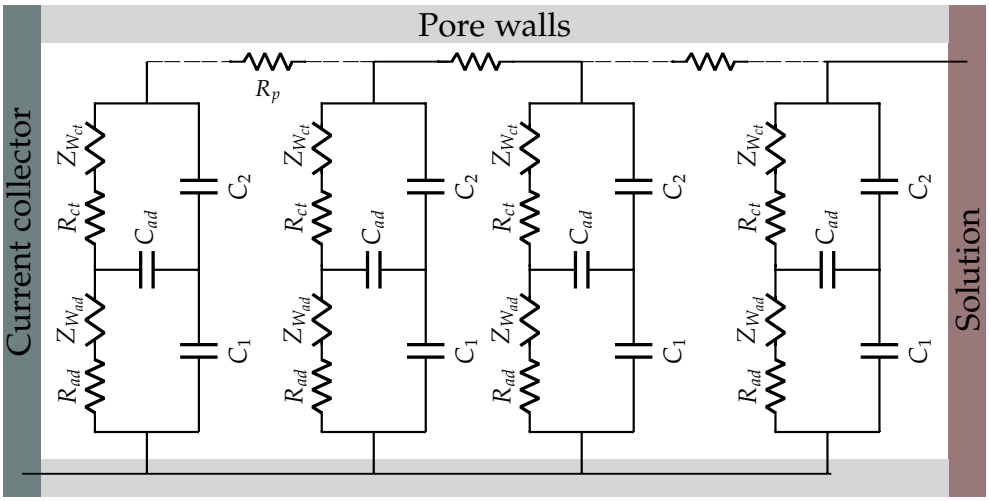

Figure 6: Equivalent circuit of the porous electrode, including the impedance describing the reaction at the surface, $Z_{WE}(\omega)$.

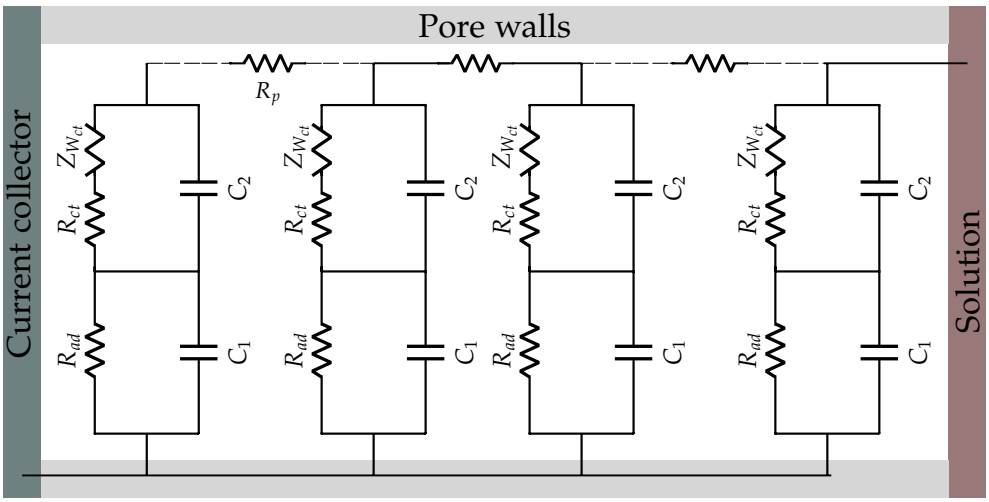

Figure 7: Equivalent circuit of the porous electrode, including the impedance describing the reaction at the surface, $Z_{WE}(\omega)$ obtained under the assumption (i) adsorption capacitance is higher than the capacitance of the inner Helmholtz plane (IHP) capacitance (ii) the mass transport in the liquid is assumed to be negligible.

3.5. Dependence of kinetic parameters on the electrode composition

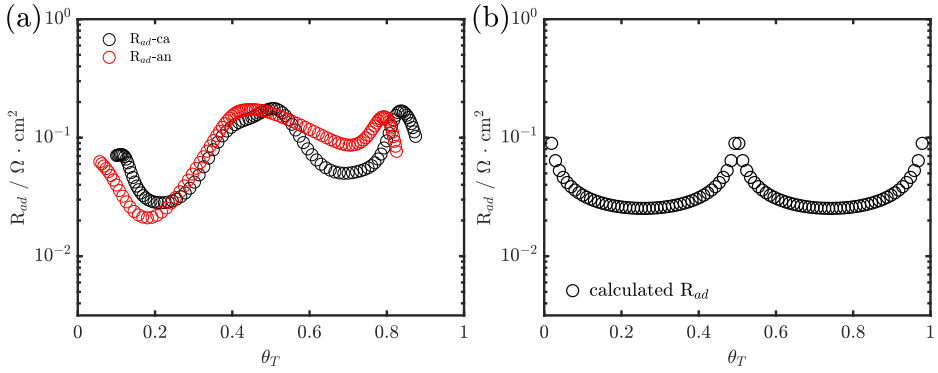

Figure 8: Dependence of the (a) the resistance of adsorption (R_{ad}) extracted from the fit (b) calculated R_{ad} using equation 8 with with $k_1^0 = 3{\cdot}10^{-6}$ cm·s^{-1} and $\alpha_1 = 0.5$ versus the total molar fraction of Li^+ in $LiMn_2O_4$ film (θ_T).

The resistance of adsorption (R_{ad}) obtained from the fit as a function of the total molar fraction of Li^+ in LMO film (θ_T) which was calculated from the charge in the voltage sweep is shown in Fig. 8a. The result indicates that R_{ad} depends on θ_T with two minima, corresponding to the peaks in the voltammogram which has been attributed to the two solid solutions in the LMO. This compositional dependence of R_{ad} can be explained by the term $[1-\beta_i]^{1-\alpha_1}\beta_i^{\alpha_1}$ in the equation describing R_{ad} of the two-stage intercalation model [34]:

$$R_{ad} = \frac{RT}{F^2 k_1^0 \left[\frac{C_{Li_e^+}}{C_0}\right]^{1-\alpha_1} [1-\beta_i]^{1-\alpha_1}\beta_i^{\alpha_1}} \tag{8}$$

where k_1^0 is the standard rate constant of the (de)solvation step, $C_{Li_e^+}$ is the concentration of the lithium ion in solution, while C_0 denotes the reference concentration (1 M in this work). α_1 represents the transfer coefficient of the (de)solvation step and β_i represents the molar fraction of the adsorbed lithium in each solid solution. For each solid solution, a corresponding β_i was estimated considering the reported changes in the atomic arrangement of the surface structure which is in equilibrium with the bulk during the reversible insertion process [56, 57]. As β_i was not quantified experimentally in this work, it was estimated from the electrode potential. The result obtained indicates that β_i assumes a fractional coverage similar to θ_i, as shown in Fig. S10 in the supporting information. Details of this calculation can be found in section S6 in the supporting information. The estimated R_{ad} obtained using a fractional coverage for β_i, exhibited a compositional dependence with a minimum in each solid solution which is similar to the compositional dependence of R_{ad} extracted from fit. The time constant for the adsorption process for Li^+ in LMO film made by multi-layer PLD is consistent with time constant for the adsorption process in LMO nanoparticles in non-aqueous media [58].

R_{ct} which models the charge transfer of Li^+ in the two solid solutions of $LiMn_2O_4$ (equation 3 and equation 4) obtained from the fit as a function of θ_T is shown in Fig. 9. The result indicates that both R_{ad} and R_{ct} are in the same order of magnitude and exhibits a similar dependence on θ_T.

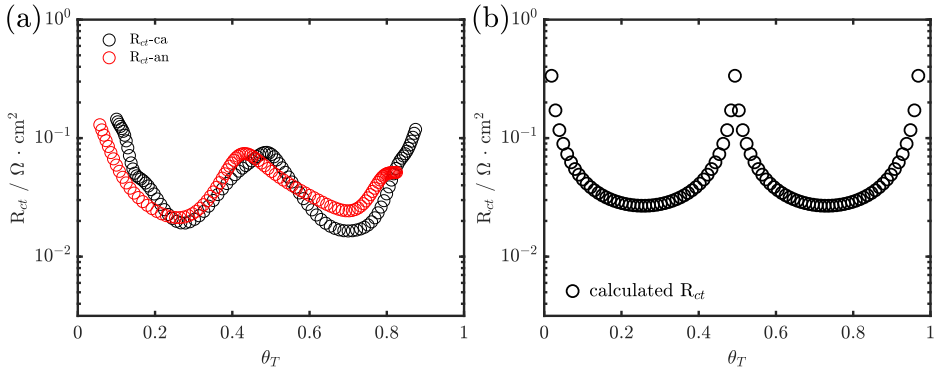

Figure 9: Compositional dependence of (a) charge transfer resistance (R_{ct}) extracted from fitting experimental data with model (b) calculated R_{ct} obtained from equation 9 with $k_2^0 = 3.10^{-6}$ cm·s^{-1} and $\alpha_2 = 0.5$.

The expression for R_{ct} from the two-stage intercalation mechanism in a host structure comprising of two-solid solutions is given by [34]:

$$R_{ct} = \frac{RT}{F^2 k_2^0 [1-\theta_i]^{1-\alpha_2} \beta_i^{1-\alpha_2} [1-\beta_i]^{\alpha_2} \theta_i^{\alpha_2}} \tag{9}$$

where k_2^0 is the standard rate constant for the insertion step, α_2 denotes the transfer coefficient of the insertion step and θ_i denotes the molar fraction of Li^+ in each of the LMO solid solution. Equation 9 predicts a decrease of R_{ct} at the onset of the de-insertion step ($\theta_i \leqslant 0.5$), and its increase when $\theta_i \geqslant 0.5$. Moreover R_{ct} is predicted to reach a minimum when $\theta_i = 0.5$ in equation 9 assuming $\alpha_2 = 0.5$ (Fig. 9b) for each solid solution in the LMO. This assumption is valid when β_i assumes a fractional coverage similar to θ_i as shown in the supporting information. The calculated R_{ct} using equation 9 exhibited a similar dependence on θ_T as the R_{ct} obtained from the fitting (Fig 9). A similar dependence of R_{ct} on θ_T has been observed already by Marchini et.al. for the reversible insertion of Li^+ in $LiMn_2O_4$ [41].

The mass transport of Li^+ in LMO film was modelled using the finite planar Warburg impedance. This decision was based on the results of the t-test obtained for different kind of Warburg elements (infinite, finite cylindrical, and finite spherical), as explained in the supporting information. The finite Warburg impedance is described as [34, 48, 59]:

$$Z_{Wct} = \sigma_{ct} \sqrt{\tau} \cdot \left[\frac{1}{\sqrt{j\tilde{\omega}}} \coth(\sqrt{j\tilde{\omega}}) \right] \tag{10}$$

where $\tilde{\omega}$ is the diffusion characteristic frequency ($\tilde{\omega} = \omega\tau$) and τ is the diffusion time constant and can be described as $\tau = l^2/D_{\theta_i}$ where l is the diffusion path length and D_{θ_i} is the diffusion coefficient of the cation in the solid. At low frequencies, when $\tilde{\omega} \ll 1$, equation 10 is reduced to [34, 59, 48]:

$$Z_{Wct} = \frac{\sigma_{ct}\sqrt{\tau}}{3} - j\frac{\sigma_{ct}}{\omega\sqrt{\tau}} \tag{11}$$

The real part ($\sigma_{ct}\sqrt{\tau}/3$) goes to a constant value at low frequencies and the mass transport

in the solid is then described by the second term in equation 11 ($\sigma_{ct}/\sqrt{\tau}$) which is a pseudo-capacitance (C_w). σ_{ct} obtained from the model can be described as [34]:

$$\sigma_{ct} = \frac{RT}{F^2}\frac{1}{\sqrt{D_{\theta_i}}}\frac{1}{(1-\theta_i)\theta_i} \tag{12}$$

Subsequently C_w can be described using the equation below:

$$C_w = \frac{RT}{F^2}\frac{1}{l}\frac{1}{(1-\theta_i)\theta_i} \tag{13}$$

C_w calculated from σ_{ct} and τ extracted from the fit was observed to have a similar shape to the current in the voltammogram as seen in Fig. 10. This is attributed to the term $(1-\theta_i)\theta_i$ in equation 13.

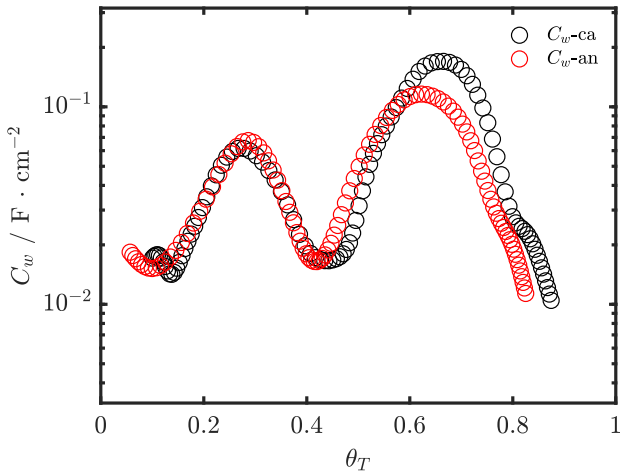

Figure 10: (a) Plot of the pseudo-capacitance (C_w) versus the total molar fraction of Li^+ in $LiMn_2O_4$ (θ_T).

The hysteresis observed in the extracted kinetic parameters (R_{ad}, R_{ct} and C_w) can be attributed to the fact that concentration of the Li^+ in the liquid and in the solid at the electrode surface and the diffusion profile depends on the direction of the voltage sweep and/or scan rate. This influences the rate of intercalation process and consequently results to the hysteresis observed in the kinetic parameters (R_{ad}, R_{ct} and C_w). This hysteresis observed is consistent with reports in literature for kinetic parameters extracted from non-stationary impedance spectroscopy [23, 60, 61].

4. Conclusion

The kinetics of reversible insertion of Li^+ in 200 nm $LiMn_2O_4$ thin films made by multi-layer PLD in aqueous electrolyte was studied with DMFA. The impedance spectra obtained indicates that the reversible insertion of Li^+ in 200 nm $LiMn_2O_4$ thin films follows a two-stage intercalation mechanism which involves a (de)solvation step as the first step and a reversible insertion step as the second step. Fitting the measured impedance with a model describing the reversible

insertion process as a two-stage process resulted in a good fit. The evolution of the kinetic parameters during the non-stationary process initiated by a voltage sweep was also investigated and the result indicates that the extracted kinetic parameters depended on the electrode composition. The resistance of adsorption and the charge transfer showed two minima, in correspondence of the standard reaction potential for each stage of the lithium deintercalation from $LiMn_2O_4$. The pseudo-capacitance of the Warburg impedance also showed a dependency on the electrode composition, in which the maxima are also located close to the standard electrode potential.

Acknowledgement

The authors gratefully acknowledge the support of the European Research Council (ERC) under the European Union's Horizon 2020 research and innovation programme (grant agreement number 772579).

[1] M. Fehse, R. Trócoli, E. Hernández, E. Ventosa, A. Sepúlveda, A. Morata, A. Tarancón, An innovative multilayer pulsed laser deposition approach for limn 2 o 4 thin film cathodes, Thin Solid Films 648 (2018) 108–112. doi:10.1016/j.tsf.2018.01.015.

[2] D. Albrecht, H. Wulfmeier, H. Fritze, Preparation and characterization of c-limn 2 o 4 thin films prepared by pulsed laser deposition for lithium-ion batteries, Energy Technology 4 (12) (2016) 1558–1564. doi:10.1002/ente.201600117.

[3] B. Put, P. M. Vereecken, N. Labyedh, A. Sepulveda, C. Huyghebaert, I. P. Radu, A. Stesmans, High cycling stability and extreme rate performance in nanoscaled limn2o4 thin films, ACS applied materials & interfaces 7 (40) (2015) 22413–22420. doi:10.1021/acsami.5b06386.

[4] H. Xia, Q. Xia, B. Lin, J. Zhu, J. K. Seo, Y. S. Meng, Self-standing porous limn 2 o 4 nanowall arrays as promising cathodes for advanced 3d microbatteries and flexible lithium-ion batteries, Nano Energy 22 (2016) 475–482. doi:10.1016/j.nanoen.2016.01.022.

[5] X. Yu, X. Chen, D. B. Buchholz, Q. Li, J. Wu, P. A. Fenter, M. J. Bedzyk, V. P. Dravid, S. A. Barnett, Pulsed laser deposition and characterization of heteroepitaxial limn 2 o 4 /la 0.5 sr 0.5 coo 3 bilayer thin films as model lithium ion battery cathodes, ACS Applied Nano Materials 1 (2) (2018) 642–653. doi:10.1021/acsanm.7b00133.

[6] S. B. Tang, M. O. Lai, L. Lu, S. Tripathy, Comparative study of limn2o4 thin film cathode grown at high, medium and low temperatures by pulsed laser deposition, Journal of Solid State Chemistry 179 (12) (2006) 3831–3838. doi:10.1016/j.jssc.2006.08.025.

[7] M. M. Thackeray, Manganese oxides for lithium batteries, Progress in Solid State Chemistry 25 (1-2) (1997) 1–71. doi:10.1016/S0079-6786(97)81003-5.

[8] C. Julien, E. Haro-Poniatowski, M. Camacho-Lopez, L. Escobar-Alarcon, J. Jimenez-Jarquin, Growth of limn2o4 thin films by pulsed-laser deposition and their electrochemical properties in lithium microbatteries, Materials Science and Engineering: B 72 (1) (2000) 36–46. doi:10.1016/S0921-5107(99)00598-X.

[9] D. O'Mahony, J. Lunney, T. Dumont, S. Canulescu, T. Lippert, A. Wokaun, Laser-produced plasma ion characteristics in laser ablation of lithium manganate, Applied Surface Science 254 (4) (2007) 811–815. doi:10.1016/j.apsusc.2007.08.002.

[10] G. Zampardi, C. Batchelor-McAuley, E. Kätelhön, R. G. Compton, Lithium-Ion-Transfer Kinetics of Single LiMn ₂ O ₄ Particles, Angew. Chemie Int. Ed. 56 (2) (2017) 641–644. doi:10.1002/anie.201610485.
URL http://doi.wiley.com/10.1002/anie.201610485

[11] D. Singh, W.-S. Kim, V. Craciun, H. Hofmann, R. Singh, Microstructural and electrochemical properties of lithium manganese oxide thin films grown by pulsed laser deposition, Applied Surface Science 197-198 (2002) 516–521. doi:10.1016/S0169-4332(02)00328-8.

[12] M. Morcrette, Non-stoichiometry in limn2o4 thin films by laser ablation, Solid State Ionics 138 (3-4) (2001) 213–219. doi:10.1016/S0167-2738(00)00796-7.

[13] R. Trócoli, A. Dushina, S. Borhani-Haghighi, A. Ludwig, F. La Mantia, Effect of Pt and Au current collector in LiMn ₂ O ₄ thin film for micro-batteries, Nanotechnology 29 (3) (2018) 035404. doi:10.1088/1361-6528/aa9e33.
URL http://stacks.iop.org/0957-4484/29/i=3/a=035404?key=crossref.b971dae96911d2e9020d4e8cda85a6ee

[14] M. Morcrette, Limn2o4 thin films for lithium ion sensors, Solid State Ionics 112 (3-4) (1998) 249–254. doi:10.1016/S0167-2738(98)00231-8.

[15] I. Yamada, T. Abe, Y. Iriyama, Z. Ogumi, Lithium-ion transfer at limn2o4 thin film electrode prepared by pulsed laser deposition, Electrochemistry Communications 5 (6) (2003) 502–505. doi:10.1016/S1388-2481(03)00113-9.

[16] M. Hirayama, H. Ido, K. Kim, W. Cho, K. Tamura, J. Mizuki, R. Kanno, Dynamic structural changes at limn2o4/electrolyte interface during lithium battery reaction, Journal of the American Chemical Society 132 (43) (2010) 15268–15276. doi:10.1021/ja105389t.

[17] M. Inaba, T. Doi, Y. Iriyama, T. Abe, Z. Ogumi, Electrochemical stm observation of limn2o4 thin films prepared by pulsed laser deposition, Journal of Power Sources 81-82 (1999) 554–557. doi:10.1016/S0378-7753(99)00215-3.

[18] R. Trócoli, A. Morata, M. Fehse, M. Stchakovsky, A. Sepúlveda, A. Tarancón, High specific power dual-metal-ion rechargeable microbatteries based on limn2o4 and zinc for miniaturized applications, ACS applied materials & interfaces 9 (38) (2017) 32713–32719. doi:10.1021/acsami.7b08883.

[19] K. Dokko, M. Mohamedi, M. Umeda, I. Uchida, Kinetic study of li-ion extraction and insertion at limn[sub 2]o[sub 4] single particle electrodes using potential step and impedance methods, Journal of The Electrochemical Society 150 (4) (2003) A425. doi:10.1149/1.1556596.

[20] N. Nakayama, T. Nozawa, Y. Iriyama, T. Abe, Z. Ogumi, K. Kikuchi, Interfacial lithium-ion transfer at the limn2o4 thin film electrode/aqueous solution interface, Journal of Power Sources 174 (2) (2007) 695–700. doi:10.1016/j.jpowsour.2007.06.113.

[21] J. Ma, C. Wang, S. Wroblewski, Kinetic characteristics of mixed conductive electrodes for lithium ion batteries, Journal of Power Sources 164 (2) (2007) 849–856. doi:10.1016/j.jpowsour.2006.11.024.

[22] J.-W. Lee, S.-I. Pyun, Investigation of lithium transport through limn2o4 film electrode in aqueous lino3 solution, Electrochimica Acta 49 (5) (2004) 753–761. doi:10.1016/j.electacta.2003.09.029.

[23] A. Battistel, G. Du, F. La Mantia, On the analysis of non-stationary impedance spectra, Electroanalysis 28 (10) (2016) 2346–2353. doi:10.1002/elan.201600260.

[24] D. Koster, G. Du, A. Battistel, F. La Mantia, Dynamic impedance spectroscopy using dynamic multi-frequency analysis: A theoretical and experimental investigation, Electrochimica Acta 246 (2017) 553–563. doi:10.1016/j.electacta.2017.06.060.

[25] A. Battistel, F. La Mantia, On the physical definition of dynamic impedance: How to design an optimal strategy for data extraction, Electrochim. Acta 304 (2019) 513–520. doi:10.1016/J.ELECTACTA.2019.03.033.
URL https://www.sciencedirect.com/science/article/pii/S001346861930427X

[26] A. M. Bond, R. J. Schwall, D. E. Smith, On-line FFT faradaic admittance measurements application to A.C. cyclic voltammetry, Journal of Electroanalytical Chemistry 85 (2) (1977) 231–247. doi:10.1016/S0022-0728(77)80290-8.

[27] S. C. Creason, D. E. Smith, Fourier transform faradaic admittance measurements. I. Demonstration of the applicability of random and pseudo-random noise as applied potential signals, Journal of Electroanalytical Chemistry 36 (1). doi:10.1016/S0022-0728(72)80466-2.

[28] Z. Stoynov, B. Savova-Stoynov, T. Kossev, Non-stationary impedance analysis of lead/acid batteries, J. Power Sources 30 (1-4) (1990) 275–285. doi:10.1016/0378-7753(93)80085-4.

[29] J. Házì, D. M. Elton, W. A. Czerwinski, J. Schiewe, V. A. Vicente-Beckett, A. M. Bond, Microcomputer-based instrumentation for multi-frequency Fourier transform alternating current (admittance and impedance) voltammetry, Journal of Electroanalytical Chemistry 437 (1-2) (1997) 1–15. doi:10.1016/S0022-0728(96)05038-3.

[30] K. Darowicki, Theoretical description of the measuring method of instantaneous impedance spectra, Journal of Electroanalytical Chemistry 486 (2) (2000) 101–105. doi:10.1016/S0022-0728(00)00110-8.

[31] K. Darowicki, P. Ślepski, Dynamic electrochemical impedance spectroscopy of the first order electrode reaction, Journal of Electroanalytical Chemistry 547 (1) (2003) 1–8. doi:10.1016/S0022-0728(03)00154-2.

[32] R. L. Sacci, D. A. Harrington, Dynamic electrochemical impedance spectroscopy, in: ECS Transactions, Vol. 19, 2009, pp. 31–42. doi:10.1149/1.3247564.

[33] D. Koster, A. R. Zeradjanin, A. Battistel, F. La Mantia, Extracting the kinetic parameters of the hydrogen evolution reaction at Pt in acidic media by means of dynamic multi-frequency analysis, Electrochimica Actadoi:10.1016/J.ELECTACTA.2019.04.013.
URL https://www.sciencedirect.com/science/article/pii/S0013468619306887

[34] C. Erinmwingbovo, D. Koster, D. Brogioli, F. LaMantia, Dynamic Impedance Spectroscopy of Nickel Hexacyanoferrate Thin Films, ChemElectroChem (2019) celc.201900805doi:10.1002/celc.201900805.
URL https://onlinelibrary.wiley.com/doi/abs/10.1002/celc.201900805

[35] M. Fehse, R. Trócoli, E. Ventosa, E. Hernández, A. Sepúlveda, A. Morata, A. Tarancón, Ultrafast dischargeable limn2o4 thin-film electrodes with pseudocapacitive properties for microbatteries, ACS applied materials & interfaces 9 (6) (2017) 5295–5301. doi:10.1021/acsami.6b15258.

[36] A. Battistel, M. Fan, J. Stojadinović, F. La Mantia, Analysis and mitigation of the artefacts in electrochemical impedance spectroscopy due to three-electrode geometry, Electrochimica Acta 135 (2014) 133–138. doi:10.

1016/j.electacta.2014.05.011.
[37] G. Zampardi, E. Ventosa, F. La Mantia, W. Schuhmann, In situ visualization of li-ion intercalation and formation of the solid electrolyte interphase on tio2 based paste electrodes using scanning electrochemical microscopy, Chemical communications (Cambridge, England) 49 (81) (2013) 9347–9349. doi:10.1039/c3cc44576c.
[38] F. Mansfeld, Minimization of high-frequency phase shifts in impedance measurements, Journal of The Electrochemical Society 135 (4) (1988) 906. doi:10.1149/1.2095825.
[39] B. K. Lesel, J. S. Ko, B. Dunn, S. H. Tolbert, Mesoporous lixmn2o4 thin film cathodes for lithium-ion pseudocapacitors, ACS nano 10 (8) (2016) 7572–7581. doi:10.1021/acsnano.6b02608.
[40] M. Okubo, E. Hosono, J. Kim, M. Enomoto, N. Kojima, T. Kudo, H. Zhou, I. Honma, Nanosize effect on high-rate li-ion intercalation in licoo2 electrode, Journal of the American Chemical Society 129 (23) (2007) 7444–7452. doi:10.1021/ja0681927.
[41] F. Marchini, F. J. Williams, E. J. Calvo, Electrochemical impedance spectroscopy study of the li x mn 2 o 4 interface with natural brine, Journal of Electroanalytical Chemistry 819 (2018) 428–434. doi:10.1016/j.jelechem.2017.11.071.
[42] W. Liu, Mechanism of the electrochemical insertion of lithium into limn[sub 2]o[sub 4] spinels, Journal of The Electrochemical Society 145 (2) (1998) 459. doi:10.1149/1.1838285.
[43] D. Aurbach, M. Levi, K. Gamulski, B. Markovsky, G. Salitra, E. Levi, U. Heider, L. Heider, R. Oesten, Capacity fading of $li_xmn_2o_4$ spinel electrodes studied by XRD and electroanalytical techniques, Journal of Power Sources 81-82 (1999) 472–479. doi:10.1016/S0378-7753(99)00204-9.
[44] G. Che, Chemical-Vapor Deposition-Based Template Synthesis of Microtubular TiS[sub 2] Battery Electrodes, Journal of The Electrochemical Societydoi:10.1149/1.1838181.
[45] M. Sofia Palagonia, C. Erinmwingbovo, D. Brogioli, F. La Mantia, Comparison between cyclic voltammetry and differential charge plots from galvanostatic cycling, Journal of Electroanalytical Chemistrydoi:10.1016/j.jelechem.2019.05.052.
[46] N. Li, C. J. Patrissi, G. Che, C. R. Martin, Rate Capabilities of Nanostructured LiMn[sub 2]O[sub 4] Electrodes in Aqueous Electrolyte, Journal of The Electrochemical Societydoi:10.1149/1.1393483.
[47] Z. Gao, J. Bobacka, A. Ivaska, Electrochemical impedance spectroscopy of cobalt(ii)-hexacyanoferrate film modified electrodes, Electrochimica Acta 38 (2-3) (1993) 379–385. doi:10.1016/0013-4686(93)85154-Q.
[48] J. Song, M. Z. Bazant, Effects of Nanoparticle Geometry and Size Distribution on Diffusion Impedance of Battery Electrodes, Journal of The Electrochemical Society 160 (1) (2013) A15–A24. doi:10.1149/2.023301jes.
URL http://jes.ecsdl.org/lookup/doi/10.1149/2.023301jes
[49] P. BRUCE, M. SAIDI, A two-step model of intercalation, Solid State Ionics 51 (3-4) (1992) 187–190. doi:10.1016/0167-2738(92)90198-X.
[50] S. Kobayashi, Y. Uchimoto, Lithium ion phase-transfer reaction at the interface between the lithium manganese oxide electrode and the nonaqueous electrolyte, The journal of physical chemistry. B 109 (27) (2005) 13322–13326. doi:10.1021/jp044283j.
[51] M. Nakayama, H. Ikuta, Y. Uchimoto, M. Wakihara, Study on the ac impedance spectroscopy for the li insertion reaction of li x la 1/3 nbo 3 at the electrode−electrolyte interface, The journal of physical chemistry. B 107 (38) (2003) 10603–10607. doi:10.1021/jp036059k.
[52] E. E. Levin, S. Y. Vassiliev, V. A. Nikitina, Solvent effect on the kinetics of lithium ion intercalation into LiCoO2, Electrochimica Acta 228 (2017) 114–124. doi:10.1016/J.ELECTACTA.2017.01.040.
URL https://www.sciencedirect.com/science/article/pii/S0013468617300403
[53] S. Y. Vassiliev, V. V. Sentyurin, E. E. Levin, V. A. Nikitina, Diagnostics of lithium-ion intercalation rate-determining step: Distinguishing between slow desolvation and slow charge transfer, Electrochimica Acta 302 (2019) 316–326. doi:10.1016/J.ELECTACTA.2019.02.043.
URL https://www.sciencedirect.com/science/article/pii/S0013468619302865
[54] M. A. Kebede, M. J. Phasha, N. Kunjuzwa, L. J. le Roux, D. Mkhonto, K. I. Ozoemena, M. K. Mathe, Structural and electrochemical properties of aluminium doped LiMn2O4 cathode materials for Li battery: Experimental and ab initio calculations, Sustain. Energy Technol. Assessments 5 (2014) 44–49. doi:10.1016/J.SETA.2013.11.005.
URL https://www.sciencedirect.com/science/article/pii/S2213138813000829
[55] F. La Mantia, J. Vetter, P. Novák, Impedance spectroscopy on porous materials: A general model and application to graphite electrodes of lithium-ion batteries, Electrochimica Acta 53 (12) (2008) 4109–4121. doi:10.1016/j.electacta.2007.12.060.
[56] C. D. Amos, M. A. Roldan, M. Varela, J. B. Goodenough, P. J. Ferreira, Revealing the Reconstructed Surface of Li[Mn ₂]O ₄, Nano Lett. 16 (5) (2016) 2899–2906. doi:10.1021/acs.nanolett.5b03926.
URL http://pubs.acs.org/doi/10.1021/acs.nanolett.5b03926
[57] D. Tang, Y. Sun, Z. Yang, L. Ben, L. Gu, X. Huang, Surface Structure Evolution of LiMn ₂ O ₄ Cathode Material upon Charge/Discharge, Chem. Mater. 26 (11) (2014) 3535–3543. doi:10.

1021/cm501125e.
URL http://pubs.acs.org/doi/10.1021/cm501125e
[58] S. Kobayashi, Y. Uchimoto, Lithium ion phase-transfer reaction at the interface between the lithium manganese oxide electrode and the nonaqueous electrolyte, Journal of Physical Chemistry B 109 (27) (2005) 13322–13326. doi:10.1021/jp044283j.
[59] A. Lasia, Electrochemical impedance spectroscopy and its applications, Springer, New York, 2014.
[60] M. Itagaki, K. Honda, Y. Hoshi, I. Shitanda, In-situ EIS to determine impedance spectra of lithium-ion rechargeable batteries during charge and discharge cycle, J. Electroanal. Chem. 737 (2015) 78–84. doi:10.1016/j.jelechem.2014.06.004.
[61] T. Pajkossy, Dynamic electrochemical impedance spectroscopy of quasi-reversible redox systems. Properties of the Faradaic impedance, and relations to those of voltammograms, Electrochim. Acta 308 (2019) 410–417. doi:10.1016/j.electacta.2019.03.197.